

Strain accommodation through facet matching in $\text{La}_{1.85}\text{Sr}_{0.15}\text{CuO}_4/\text{Nd}_{1.85}\text{Ce}_{0.15}\text{CuO}_4$ ramp-edge junctions

Cite as: APL Mater. **3**, 086101 (2015); <https://doi.org/10.1063/1.4927796>

Submitted: 24 April 2015 . Accepted: 22 July 2015 . Published Online: 03 August 2015

M. Hoek , F. Coneri, N. Poccia, X. Renshaw Wang, X. Ke, G. Van Tendeloo, and H. Hilgenkamp



View Online



Export Citation



CrossMark

ARTICLES YOU MAY BE INTERESTED IN

[A new form of \$\text{Ca}_3\text{P}_2\$ with a ring of Dirac nodes](#)

APL Materials **3**, 083602 (2015); <https://doi.org/10.1063/1.4926545>

[Perspective: Rapid synthesis of complex oxides by combinatorial molecular beam epitaxy](#)

APL Materials **4**, 053205 (2016); <https://doi.org/10.1063/1.4943989>

[On the nature of ionic liquid gating of \$\text{Nd}_{2-x}\text{Ce}_x\text{CuO}_4\$ thin films](#)

Low Temperature Physics **43**, 290 (2017); <https://doi.org/10.1063/1.4976636>

additive manufacturing epitaxial crystal growth cerium oxide polishing powder silver nanoparticles sputtering targets III-IV semiconductors CVD precursors europium phosphors

AMERICAN ELEMENTS

THE ADVANCED MATERIALS MANUFACTURER®

deposition slugs OLED Lighting spintronics solar energy osmium nanoribbons thin films chalcogenides AuNPs GDC Li-ion battery electrolytes 99.999% ruthenium spheres

endohedral fullerenes copper nanoparticles diamond micropowder CIGS MBE grade materials palladium catalysts flexible electronics beta-barium borate borosilicate glass dysprosium pellets YBCO pyrolytic graphite 3d graphene foam indium tin oxide mesoporous silica raman substrates sapphire windows tungsten carbide InGaAs barium fluoride carbon nanotubes lithium niobate scandium powder

gallium lump glassy carbon nanodispersions surface functionalized nanoparticles organometallics quantum dot

perovskite crystals yttrium iron garnet alternative energy h-BN gold nanocubes graphene oxide macromolecules photonics rhodium sponge fiber optics beamsplitters infrared dyes zeolites fused quartz metallocenes platinum ink buckyballs Ti-6Al-4V

Now Invent.™
The Next Generation of Material Science Catalogs

American Elements opens up a world of possibilities so you can **Now Invent!**

Over 15,000 certified high purity laboratory chemicals, metals, & advanced materials and a state-of-the-art Research Center. Printable GHS-compliant Safety Data Sheets. Thousands of new products. And much more. All on a secure multi-language "Mobile Responsive" platform.

www.americanelements.com

APL Mater. **3**, 086101 (2015); <https://doi.org/10.1063/1.4927796>

3, 086101

© 2015 Author(s).

Strain accommodation through facet matching in $\text{La}_{1.85}\text{Sr}_{0.15}\text{CuO}_4/\text{Nd}_{1.85}\text{Ce}_{0.15}\text{CuO}_4$ ramp-edge junctions

M. Hoek,^{1,a} F. Coneri,¹ N. Poccia,¹ X. Renshaw Wang,^{1,b} X. Ke,² G. Van Tendeloo,² and H. Hilgenkamp^{1,c}

¹MESA+ Institute for Nanotechnology, University of Twente, P.O. Box 217, 7500 AE Enschede, The Netherlands

²Electron Microscopy for Materials Science (EMAT), Department of Physics, University of Antwerp, Groenenborgerlaan 171, B-2020 Antwerp, Belgium

(Received 24 April 2015; accepted 22 July 2015; published online 3 August 2015)

Scanning nano-focused X-ray diffraction and high-angle annular dark-field scanning transmission electron microscopy are used to investigate the crystal structure of ramp-edge junctions between superconducting electron-doped $\text{Nd}_{1.85}\text{Ce}_{0.15}\text{CuO}_4$ and superconducting hole-doped $\text{La}_{1.85}\text{Sr}_{0.15}\text{CuO}_4$ thin films, the latter being the top layer. On the ramp, a new growth mode of $\text{La}_{1.85}\text{Sr}_{0.15}\text{CuO}_4$ with a 3.3° tilt of the c -axis is found. We explain the tilt by developing a strain accommodation model that relies on facet matching, dictated by the ramp angle, indicating that a coherent domain boundary is formed at the interface. The possible implications of this growth mode for the creation of artificial domains in morphotropic materials are discussed. © 2015 Author(s). All article content, except where otherwise noted, is licensed under a Creative Commons Attribution 3.0 Unported License. [<http://dx.doi.org/10.1063/1.4927796>]

Ramp-edge junction technology is an integral part of the research into the properties of (high- T_c) superconductors.¹ The ramp-edge configuration provides a good platform to create ab -plane junctions between high- T_c superconductors and between high- T_c and conventional superconductors.^{2,3} Additionally, ramp-edges are also used to create junctions through graphoepitaxy, where a large lattice mismatch between substrate and film causes the film to grow following the surface normal instead of the crystal direction of the substrate.⁴ In this letter, we show that there can be a third kind of junction that is not quite a full ab -plane contact and where strain does play a role in determining the details of the growth, but not to the extent of promoting graphoepitaxy. We find that for appropriate lattice mismatches, a tilted phase can form on the ramp with respect to the c -axis aligned phase that grows away from the ramp; the tilting is dictated by facet matching to the lattice planes exposed on the ramp-edge, and is proportional to the ramp angle.

We have fabricated ramp-edge junctions between superconducting $\text{Nd}_{1.85}\text{Ce}_{0.15}\text{CuO}_4$ (NCCO) and $\text{La}_{1.85}\text{Sr}_{0.15}\text{CuO}_4$ (LSCO) on $[\text{LaAlO}_3]_{0.3}[\text{Sr}_2\text{AlTaO}_6]_{0.7}$ (LSAT) substrates using pulsed laser deposition (PLD), standard photolithography, and *ex situ* and *in situ* argon ion milling. The samples are grown from commercial and homemade polycrystalline PLD targets. The NCCO layer is grown from a target with extra copper added to suppress a parasitic $(\text{Nd,Ce})_2\text{O}_3$ (CNO) phase.⁵ We use a specifically tailored oxygen annealing and reduction procedure to ensure both layers are superconducting.^{5,6} A schematic view of the junction cross-section is shown in the inset of Fig. 1. The junction consists of a NCCO bottom electrode sandwiched between undoped Nd_2CuO_4 (NCO) layers in which a ramp is defined by *ex situ* argon ion milling under an angle of 45° . The NCO layers act as a buffer layer and a capping layer. The LSCO top electrode is deposited after an extra *in situ* cleaning step of hard and soft argon ion milling. The final devices are structured for

^aCurrently at Boston College, 140 Commonwealth Ave, Chestnut Hill, Massachusetts 02467, USA.

^bCurrently at MIT, 77 Massachusetts Ave, Cambridge, Massachusetts 02139, USA.

^cAuthor to whom correspondence should be addressed. Electronic mail: h.hilgenkamp@utwente.nl.

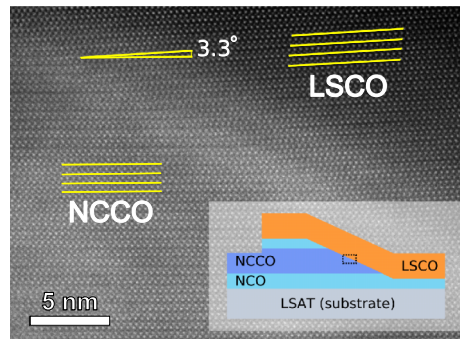


FIG. 1. HAADF-STEM characterization of the LSCO/NCCO ramp-edge junctions. The inset shows a schematic cross-section of the device, the bottom electrode consists of 70 nm Nd_2CuO_4 (NCO), 150 nm $\text{Nd}_{1.85}\text{Ce}_{0.15}\text{CuO}_4$ (NCCO), and 20 nm NCO, the top electrode consists of 150 nm $\text{La}_{1.85}\text{Sr}_{0.15}\text{CuO}_4$ (LSCO). The HAADF-STEM image shows a close-up of the ramp area (indicated by the dotted box in the inset), the NCCO and LSCO *ab*-planes are indicated by yellow lines. The LSCO top layer is tilted with respect to the NCCO lattice by 3.3° .

electronic transport measurements, described elsewhere.^{6,7} Here, we focus on the structural characterization of the interface between NCCO and LSCO in the ramp area of the junctions. We employ two different techniques to probe the interface: scanning nano-focused X-ray diffraction (nXRD) and high-angle annular dark-field scanning transmission electron microscopy (HAADF-STEM). The former has become a powerful tool for selective analysis thanks to the development of high brilliance synchrotron sources that employ micro and nano-focused beams.⁸ This allows nXRD to combine sub-micron lateral resolution with high *k*-space resolution^{9–17} for the nondestructive study of the crystal structures of buried layers. HAADF-STEM complements the nXRD measurements by providing a local cross-section of Z contrast with atomic resolution. More details on sample fabrication and the HAADF-STEM and nXRD measurement setups can be found in the supplementary material.¹⁸

Fig. 1 shows a HAADF-STEM close-up of the ramp interface. The NCCO and LSCO layers can be identified, as well as a tilting of the LSCO lattice, indicated with yellow lines. The layer composition is verified by electron diffraction and energy dispersive X-ray spectroscopy (EDX), discussed in more detail elsewhere.^{6,7} The exact tilting of the LSCO lattice is determined by looking at the Fourier transforms of the NCCO and the LSCO lattices and is found to be 3.3° on the central part of the ramp.

Next, we use nXRD to show that the tilting of the LSCO lattice is not a local effect, but occurs along the entire ramp. Fig. 2 summarizes the nXRD results. A CCD camera collects two dimensional X-ray spectra in a grid scan across the junction interface with the beam aligned to

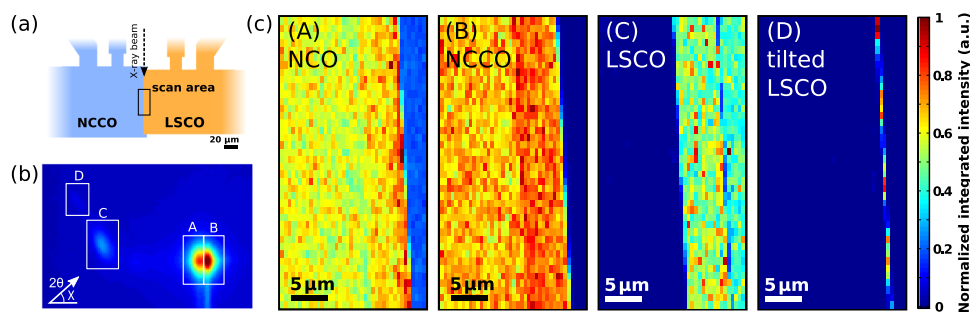


FIG. 2. Nano-scale X-ray diffraction structural mapping. (a) Schematic top view of the junction with the scan area and the beam direction indicated. (b) Detector image zoomed around the NCO, NCCO, and LSCO (1 0 7) peaks. The white boxes are used in the integration for (c). (c) Integrated nXRD intensity maps for NCO (A), NCCO (B), LSCO (C), and a tilted phase of LSCO (D), only visible at the ramp, measured on the scan area indicated in (a). A background is subtracted from all maps and the signal is normalized to the highest intensity pixel. The pixel size is $0.5 \mu\text{m} \times 1 \mu\text{m}$, shortest in the horizontal direction.

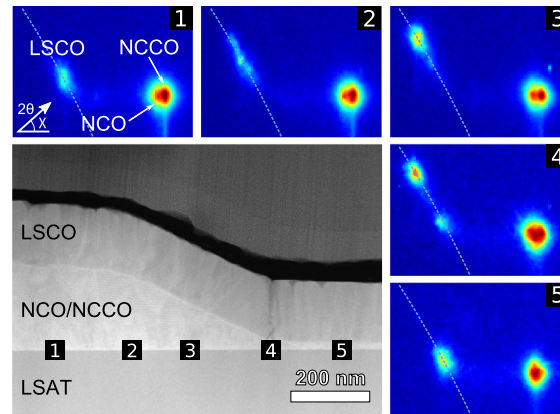


FIG. 3. LSCO lattice tilting, the bottom left panel shows a low magnification HAADF-STEM cross-section of the sample with five regions indicated. The NCCO and LSCO layers are labeled as well as the LSAT substrate (the NCO layers are not indicated for clarity). The structure is capped with carbon, and electron and ion-deposited Pt layers. The nXRD frames surrounding the HAADF-STEM image show the diffraction pattern for NCO (1 0 7), NCCO (1 0 7), and LSCO (1 0 7) for the five approximate regions. The diffraction patterns show a gradual change to a tilted phase going from 1 to 3 and an abrupt transition from the tilted phase to the c -axis aligned phase at the grain boundary near region 4. The dashed line follows a constant 2θ angle.

NCCO (008), which corresponds to a beam angle of around 16° . The images in Fig. 2(b) and Fig. 3(1–5) show the diffraction pattern as it appears on the CCD camera. The horizontal direction on the detector corresponds with the l Miller index and the vertical direction with the h Miller index. Concentric circles around the direct beam are lines of equal 2θ , where the inclination with respect to the horizontal axis corresponds to a tilting or a non-zero χ angle. Fig. 2(a) shows the measurement geometry, the scan area being $20\ \mu\text{m} \times 40\ \mu\text{m}$. The focus of the beam allows for the collection of a broader range of Bragg reflections, including (1 0 7), which shows a larger and clearer peak separation. Fig. 2(b) shows a summation of all the frames collected in one scan zoomed in on the (1 0 7) reflections of NCO, NCCO and LSCO, and the tilted LSCO phase, labeled A–D. Fig. 2(c) shows intensity maps of the scan area by integrating over the white boxes labeled A–D in Fig. 2(b). For the mapping, a constant background is subtracted and the images are normalized to the highest intensity pixel, more details can be found in the supplementary material.¹⁸ The pixel size is $0.5\ \mu\text{m} \times 1\ \mu\text{m}$, with the shortest size in the horizontal direction; each panel is constructed from 1600 diffraction patterns. In Fig. 2(c), the device architecture of Fig. 1 can be identified. For NCO, panel A in Fig. 2(c), going from left to right, first the NCO layer underneath the NCCO electrode is imaged. Then the junction overlap area, defined by the complete NCO/NCCO/NCO/LSCO stack, is visible; it has a higher intensity, because here the NCO capping layer has not been etched away (see the inset of Fig. 1). The ramp is identified as the step-like intensity change from orange to light blue in 1–2 pixels, comparable to the width of the ramp ($\sim 300\ \text{nm}$). Finally, beyond the ramp on the right, finite intensity remains as the etching process of the ramp is stopped in the NCO layer. In the mapping of NCCO, panel B, both the overlap area and the ramp can be identified. The overlap area shows a higher intensity because the NCCO outside the overlap area is etched away slightly during the definition of the LSCO contact and the removal of the NCO capping layer. Beyond the ramp, only background intensity remains. For LSCO, panel C, we get a complementary picture; the overlap area can be identified and no intensity remains to the left of the overlap area, where all the LSCO has been etched away. The slightly higher intensity for the overlap area can be explained by a higher crystal quality of LSCO on the overlap as compared to the LSCO grown on the etched surface of NCO on the right side of the ramp. At the position where the ramp can be identified in the NCO and NCCO maps, we observe missing intensity in the LSCO map. Part of the LSCO (1 0 7) intensity shifts on the detector. Panel D shows a mapping of the intensity of this shifted phase. Here, the intensity along the ramp corresponds to the missing intensity in panel C. We observe the same shift for all peaks attributed to LSCO, i.e., (008), (1 0 7), and $(\bar{1}\ 0\ 5)$, indicating that the effect is not caused by a rotation of the sample with respect to the beam, see the supplementary material.¹⁸

In the shift, the 2θ angle does not change, this excludes lattice deformation as the origin of the shift, since that would be accompanied by a change in c -axis length. We therefore attribute the shift of the LSCO peaks to a tilting of the LSCO lattice, while the LSCO unit cell remains unchanged. The tilt is measured to be around 3° from the shift of the (008), (107), and ($\bar{1}$ 05) peaks of LSCO, see Fig. S2 in the supplementary material.¹⁸ This is close to the 3.3° tilting measured using HAADF-STEM, see Fig. 1.

In the grid scan for Fig. 2(c), the beam crosses the ramp at a small angle, which allows us to image effects on different parts of the ramp despite the spot size being comparable to the size of the ramp. Fig. 3 visualizes the tilting of the LSCO lattice as the X-ray beam is scanned across the junction. Panels 1 to 5 in Fig. 3 show the (107) diffraction peaks for NCO, NCCO, and LSCO corresponding to different areas of the ramp-edge structure, their approximate location indicated by the numbers 1–5 in the HAADF-STEM image. The dashed line in the detector images is a section of a circle of constant 2θ angle, defined by the direct beam center and the main LSCO (107) peak. The LSCO (107) peak can be seen to shift in different ways at the top and the bottom of the ramp. Panel 2 corresponds to the top of the ramp structure where a gradual change in the ramp angle results in a spread-out peak structure. On the ramp, only the 3.3° tilted phase is observed (panel 3). At the bottom of the ramp, the tilted phase meets the c -axis aligned phase in a grain boundary. This is reflected in panel 4, where two distinct peaks are observed, with only small streaking between the two. Finally, in panel 5, just as in panel 1, the LSCO is fully c -axis aligned again.

The tilting observed in our experiment is different from graphoepitaxy that is known to occur in ramp-edge structures of cuprate superconductors.⁴ In graphoepitaxy, $\text{YBa}_2\text{Cu}_3\text{O}_{7-x}$ (YBCO), for example, can grow on a ramp etched into a MgO substrate, where the YBCO tilting follows the ramp angle, creating Josephson junctions at the top and bottom of the ramp.^{4,19} For our junctions, the tilt does not follow the ramp angle directly, but is much smaller than the ramp angle. We argue that the tilting of the LSCO lattice on the ramp is induced by strain at the interface. The tilted phase has a better lattice match along the NCCO facets exposed on the ramp than a c -axis aligned phase. Tilting to accommodate lattice mismatch is observed in semiconductor heterostructures for large lattice mismatches in combinations like MnAs/GaAs, GaN/GaAs, GaAs/Si, Cu/GaAs, or α - $\text{Si}_3\text{N}_4/\text{Si}$.^{20–23} Here, the tilt is determined by the lattice mismatch and the vicinal angle of the substrate. In our case, the tilting is determined by the angle of the ramp. From HAADF-STEM and atomic force microscopy, we measure a ramp angle of around 26° , the facet closest to this angle is NCCO (3019), using literature values for NCCO.²⁴ The corresponding LSCO (3019) plane has an incline of about 29° ,²⁵ which gives a 3° incline for the (001) planes, when the unit cell is tilted to make the (3019) planes of NCCO and LSCO parallel. The lattice mismatch between LSCO (3019) and NCCO (3019) along the ramp is 1.7% versus an in-plane mismatch of 4.4% for c -axis aligned growth. Other planes like (106), (107), (2013), and (3020) also have an incline close to 26° . For all these planes, the corresponding LSCO plane is tilted by about 3° and the lattice mismatch is always less than 2%.

In Fig. 3, we have seen that a gradual change of the ramp angle at the top of the ramp leads to a range of tilt angles for the tilted LSCO phase. The changing ramp angle exposes different facets of NCCO, which results in LSCO layers with a different tilt. Assuming that for each angle the Miller indices of the aligned NCCO and LSCO planes are the same, the tilt angle γ is given by

$$\gamma = \arctan\left(\frac{a_N c_L}{c_N a_L} \tan \alpha\right) - \alpha, \quad (1)$$

where α is the ramp angle in degrees and $a(c)_{N,L}$ is the a (c)-axis length of NCCO (N) and LSCO (L). A full derivation can be found in the supplementary material.¹⁸ We can extract the ratios a_N/a_L and c_L/c_N in Eq. (1) from the HAADF-STEM image of Fig. 1. By focusing on the ratios we can minimize errors due to image distortion. We find $a_N/a_L = 1.05$ and $c_L/c_N = 1.098$, to be compared to 1.046 and 1.095, respectively, when using the literature values.^{24,25} Fig. 4(a) schematically shows the tilting process and in Fig. 4(b) the blue curve (left axis) shows the dependence of Eq. (1) using the measured ratios. The orange curve (right axis) shows the difference between the absolute lattice mismatch for the tilted phase (see supplementary material¹⁸) and the in-plane absolute lattice

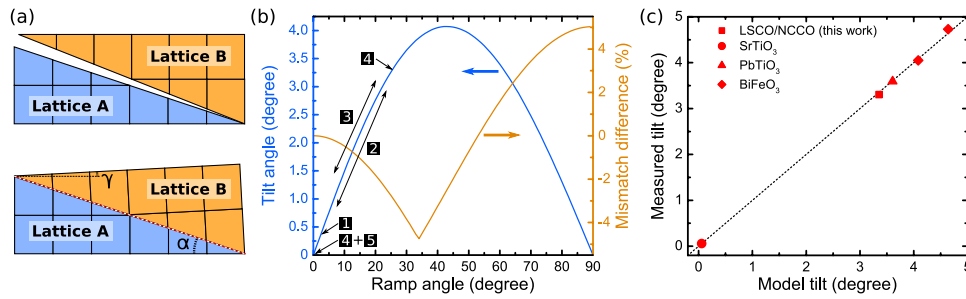


FIG. 4. Strain accommodation model for lattice tilt on a ramp interface. (a) Schematic representation of the tilting process for two lattices A and B with an in-plane lattice mismatch and different c/a ratios. The ramp angle α and the tilt angle γ are indicated. (b) Modelled tilt of the LSCO phase on the NCCO ramp toward the top of the ramp as a function of ramp angle following Eq. (1) using the measured a_N/a_L and c_L/c_N ratios (blue curve, left axis). The approximate location of the tilt in regions 1–5 of Fig. 3 is indicated, where 2 and 3 cover a range of tilt angles. The other curve shows the absolute lattice mismatch difference between the tilted phase and a c -axis oriented phase, where a negative value indicates a lower mismatch for the tilted phase (orange curve, right axis). (c) Experimental tilt versus model tilt using Eq. (1) for various oxide systems. The data points for SrTiO_3 , PbTiO_3 , and BiFeO_3 are determined using information from the main text and the TEM measurements in Refs. 32–34. The dotted line indicates the predicted tilt.

mismatch for the c -axis-aligned phase ($|a_N - a_L|/a_N$); a negative value indicates that the tilted phase has a favorable, lower lattice mismatch.

For a ramp angle of 26° (1°), we predict a tilt of 3.35° (0.1°), where the error bar is mostly generated by inaccuracy in determining the ramp angle. This value falls within the measurement error bar for the measured 3.3° tilt. The tilt ranges associated with panels 1–5 in Fig. 3 are schematically indicated in Fig. 4(b). This leads us to conclude that the facet matching model can qualitatively describe the LSCO tilt over the whole ramp structure and quantitatively predict the tilt angle for the dominant ramp angle.

It is interesting to see what Eq. (1) predicts for other materials commonly used in ramp-edge junctions. Most junction designs work with YBCO, which has a c/a ratio very comparable to the electron doped cuprates. In the configuration of YBCO/NCCO²⁶ or for NCCO as interlayer in YBCO–YBCO Josephson junctions,²⁷ the predicted tilt is small, $<0.3^\circ$, and it results in an unfavorable lattice mismatch compared to c -axis aligned growth. The same holds for other common interlayer materials like $\text{PrBa}_2\text{Cu}_3\text{O}_{7-x}$ ²⁸ and for YBCO grown on ramps etched into substrates like LaAlO_3 ²⁹ or MgO ,⁴ where in the latter case graphoepitaxy is found due to the large in-plane lattice mismatch. A scenario similar to LSCO/NCCO is found in the combination of YBCO and LSCO. Our model predicts a tilt of 3.45° for LSCO/YBCO and -3.16° for YBCO/LSCO for a ramp angle of 26° . These material combinations have been studied by the Maeda group,^{30,31} but no reports on the structure are available.

We note that lattice tilting is also observed across grain boundaries in other oxide systems, for example, across a twin grain boundary in tetragonal SrTiO_3 ³² or PbTiO_3 .³³ In both cases, the tilting can be described using a simplified version of Eq. (1), since across the domain wall a and c are exchanged and the “ramp” angle can be defined by $\arctan(a/c)$, leading to $\gamma = 2 \arctan(c/a) - 90^\circ$. A tilted lattice also appears across a grain boundary between rhombohedrally distorted (R) and tetragonally distorted (T) BiFeO_3 for specific substrate strain.^{34–36} Here, Eq. (1) can be used directly by using the pseudocubic c/a ratios associated with the R and the T -phase and taking the inclination of the grain boundary as the ramp angle. Fig. 4(c) shows the measured lattice tilt versus the predicted lattice tilt using Eq. (1) for the three materials described above and the LSCO/NCCO system described in this letter. The measured tilt and the model tilt are determined using the main text and the TEM figures in Refs. 32–34. The two data points for BiFeO_3 correspond to the T/R and the R/T configurations. The dotted line indicates the predicted tilt; it is clear that the lattice tilt in all four systems can be well described with the facet matching model for strain accommodation. Conversely, it also means that the LSCO/NCCO ramp-edge junctions have a crystalline grain boundary contact at the interface. First, this is important for the electronic measurements discussed elsewhere,^{6,7} but second, it also means that a ramp-edge structure can potentially be used

to tailor specific, artificial grain boundaries in piezoelectric materials like BiFeO₃ to enhance their piezoelectric properties. A periodic mesa structure in SrTiO₃ with ramps on both sides could yield an artificial realization of the mixed phase state as observed by Zeches *et al.*³⁴

In summary, nano-focused XRD has allowed us to identify a tilted phase of LSCO in LSCO/NCCO ramp-edge junctions, also confirmed by HAADF-STEM. We argue that the origin of the tilting is an interplay between lattice strain and the ramp angle, promoting the LSCO to nucleate in a tilted phase on the exposed NCCO facets at the ramp interface. Our facet matching model successfully predicts this behavior for material combinations that have a sufficiently large in-plane lattice mismatch and have a different c/a ratio, with a potential application in realizing artificial domain wall structures in piezoelectric materials.

This research was supported by the Dutch NWO foundation through a VICI grant. X.R.W. is supported by an NWO Rubicon Grant (2011, No. 680-50-1114). N.P. is supported by a Marie Curie grant. The nXRD experiments were performed on the ID13 beamline at the European Synchrotron Radiation Facility (ESRF), Grenoble, France; we are grateful to M. Burghammer, E. Di Cola, and G. Campi for providing assistance in using beamline ID13. Part of the research leading to these results has received funding from the European Union Seventh Framework Programme under Grant Agreement No. 312483 - ESTEEM2 (Integrated Infrastructure Initiative-I3). X.K. and G.v.T. acknowledge funding from the European Research Council under the Seventh Framework Program (FP7) ERC Grant No. 246791-COUNTATOMS. The authors thank S. Harkema for valuable discussion.

- ¹ J. Gao, W. Aarnink, G. Gerritsma, and H. Rogalla, *Physica C* **171**, 126 (1990).
- ² H. Hilgenkamp and J. Mannhart, *Rev. Mod. Phys.* **74**, 485 (2002).
- ³ F. Tafuri and J. J. R. Kirtley, *Rep. Prog. Phys.* **68**, 2573 (2005).
- ⁴ M. Faley, U. Poppe, R. Dunin-Borkowski, M. Schiek, F. Boers, H. Chocholacs, J. Dammers, E. Eich, N. Shah, A. Ermakov, V. Slobodchikov, Y. Maslennikov, and V. Koshelets, *IEEE Trans. Appl. Supercond.* **23**, 1600705 (2013).
- ⁵ M. Hoek, F. Coneri, D. P. Leusink, P. D. Eerkes, X. R. Wang, and H. Hilgenkamp, *Supercond. Sci. Technol.* **27**, 044017 (2014).
- ⁶ M. Hoek, F. Coneri, X. Renshaw Wang, X. Ke, G. van Tendeloo, and H. Hilgenkamp, "Ramp-edge junctions between superconducting electron-doped Nd_{1.85}Ce_{0.15}CuO₄ and hole-doped La_{1.85}Sr_{0.15}CuO₄" (unpublished).
- ⁷ M. Hoek, "At the interface between electron and hole-doped cuprates," Ph.D. thesis, University of Twente, (2014).
- ⁸ J. Stangl, C. Mocuta, A. Diaz, T. H. Metzger, and G. Bauer, *ChemPhysChem* **10**, 2923 (2009).
- ⁹ M. Holt, K. Hassani, and M. Sutton, *Phys. Rev. Lett.* **95**, 085504 (2005).
- ¹⁰ Y. Xiao, Z. Cai, and B. Lai, *Nanotechnology* **16**, 1754 (2005).
- ¹¹ M. Hanke, M. Dubschlaff, M. Schmidbauer, T. Boeck, S. Schöder, M. Burghammer, C. Riekel, J. Patommel, and C. G. Schroer, *Appl. Phys. Lett.* **92**, 193109 (2008).
- ¹² M. Fratini, N. Poccia, A. Ricci, G. Campi, M. Burghammer, G. Aeppli, and A. Bianconi, *Nature* **466**, 841 (2010).
- ¹³ N. Hrauda, J. Zhang, E. Wintersberger, T. Etzelstorfer, B. Mandl, J. Stangl, D. Carbone, V. Holý, V. Jovanović, C. Biasotto, L. K. Nanver, J. Moers, D. Grützmacher, and G. Bauer, *Nano Lett.* **11**, 2875 (2011).
- ¹⁴ S. O. Hruszkewycz, C. M. Folkman, M. J. Highland, M. V. Holt, S. H. Baek, S. K. Streiffer, P. Baldo, C. B. Eom, and P. H. Fuoss, *Appl. Phys. Lett.* **99**, 232903 (2011).
- ¹⁵ J. A. Klug, M. V. Holt, R. N. Premnath, A. Joshi-Imre, S. Hong, R. S. Katiyar, M. J. Bedzyk, and O. Auciello, *Appl. Phys. Lett.* **99**, 052902 (2011).
- ¹⁶ N. Poccia, A. Ricci, G. Campi, M. Fratini, A. Puri, D. D. Gioacchino, A. Marcelli, M. Reynolds, M. Burghammer, N. L. Saini, G. Aeppli, and A. Bianconi, *Proc. Natl. Acad. Sci. U. S. A.* **109**, 15685 (2012).
- ¹⁷ C. V. Falub, M. Meduna, D. Chrastina, F. Isa, A. Marzegalli, T. Kreiliger, A. G. Taboada, G. Isella, L. Miglio, A. Dommann, and H. von Kanel, *Sci. Rep.* **3**, 2276 (2013).
- ¹⁸ See supplementary material at <http://dx.doi.org/10.1063/1.4927796> for details on the experimental methods and the derivation of the lattice tilt.
- ¹⁹ S. K. Streiffer, B. M. Lairson, and J. C. Bravman, *Appl. Phys. Lett.* **57**, 2501 (1990).
- ²⁰ B. W. Dodson, D. R. Myers, A. K. Datye, V. S. Kaushik, D. L. Kendall, and B. Martinez-Tovar, *Phys. Rev. Lett.* **61**, 2681 (1988).
- ²¹ F. Riesz, *Vacuum* **46**, 1021 (1995).
- ²² A. Yamada, P. J. Fons, R. Hunger, K. Iwata, K. Matsubara, and S. Niki, *Appl. Phys. Lett.* **79**, 608 (2001).
- ²³ L. Wan, J. Shangguan, H. Luo, Y. Huang, and B. Tang, *Eur. Phys. J.: Appl. Phys.* **38**, 231 (2007).
- ²⁴ H. Kimura, Y. Noda, F. Sato, K. Tsuda, K. Kurahashi, T. Uefuji, M. Fujita, and K. Yamada, *J. Phys. Soc. Jpn.* **74**, 2282 (2005).
- ²⁵ H. Palmer, C. Greaves, M. Slaski, V. Trofimova, Y. Yarmoshenko, and E. Kurmaev, *Physica C* **291**, 104 (1997).
- ²⁶ I. Takeuchi, S. N. Mao, X. X. Xi, K. Petersen, C. J. Lobb, and T. Venkatesan, *Appl. Phys. Lett.* **67**, 2872 (1995).
- ²⁷ L. Alff, U. Schoop, R. Gross, R. Gerber, and A. Beck, *Physica C* **271**, 339 (1996).
- ²⁸ J. Gao, Y. Boguslavskij, B. B. G. Klopman, D. Terpstra, G. J. Gerritsma, and H. Rogalla, *Appl. Phys. Lett.* **59**, 2754 (1991).
- ²⁹ J. Wen, N. Koshizuka, C. Traeholt, H. Zandbergen, E. Reuvekamp, and H. Rogalla, *Physica C* **255**, 293 (1995).
- ³⁰ A. Fujimaki, Y. Fukai, M. Inoue, T. Kubo, L. Gómez, and A. Maeda, in Applied Superconductivity Conference, 2006.

- ³¹ L. Gómez, T. Kubo, H. Kitano, Y. Fukai, M. Inoue, A. Maeda, and A. Fujimaki, in *The 4th International Symposium on Nanotechnology*, 2006.
- ³² M. Honig, J. A. Sulpizio, J. Drori, A. Joshua, E. Zeldov, and S. Ilani, *Nat. Mater.* **12**, 1112 (2013).
- ³³ G. Catalan, A. Lubk, A. H. G. Vlooswijk, E. Snoeck, C. Magen, A. Janssens, G. Rispens, G. Rijnders, D. H. A. Blank, and B. Noheda, *Nat. Mater.* **10**, 963 (2011).
- ³⁴ R. J. Zeches, M. D. Rossell, J. X. Zhang, A. J. Hatt, Q. He, C.-H. Yang, A. Kumar, C. H. Wang, A. Melville, C. Adamo, G. Sheng, Y.-H. Chu, J. F. Ihlefeld, R. Erni, C. Ederer, V. Gopalan, L. Q. Chen, D. G. Schlom, N. A. Spaldin, L. W. Martin, and R. Ramesh, *Science* **326**, 977 (2009).
- ³⁵ J. X. Zhang, Q. He, M. Trassin, W. Luo, D. Yi, M. D. Rossell, P. Yu, L. You, C. H. Wang, C. Y. Kuo, J. T. Heron, Z. Hu, R. J. Zeches, H. J. Lin, A. Tanaka, C. T. Chen, L. H. Tjeng, Y.-H. Chu, and R. Ramesh, *Phys. Rev. Lett.* **107**, 147602 (2011).
- ³⁶ I. C. Infante, J. Juraszek, S. Fusil, B. Dupé, P. Gemeiner, O. Diéguez, F. Pailloux, S. Jouen, E. Jacquet, G. Geneste, J. Pacaud, J. Íñiguez, L. Bellaiche, A. Barthélémy, B. Dkhil, and M. Bibes, *Phys. Rev. Lett.* **107**, 237601 (2011).